



Accuracy Verification of Multiple Floating LiDARs at the Mutsu-Ogawara Site

Uchiyama, Shogo ; Ohsawa, Teruo ; Asou, Hiroshi ; Konagaya, Mizuki ;
Misaki, Takeshi ; Araki, Ryuzo ; Hamada, Kohei

(Citation)

Energies, 17(13):3164

(Issue Date)

2024-07

(Resource Type)

journal article

(Version)

Version of Record

(Rights)

© 2024 by the authors. Licensee MDPI, Basel, Switzerland.

This article is an open access article distributed under the terms and conditions of the Creative Commons Attribution (CC BY) license


(URL)

<https://hdl.handle.net/20.500.14094/0100490467>



Article

Accuracy Verification of Multiple Floating LiDARs at the Mutsu-Ogawara Site

Shogo Uchiyama ^{1,2,*}, Teruo Ohsawa ¹, Hiroshi Asou ³, Mizuki Konagaya ^{1,4} , Takeshi Misaki ^{1,4}, Ryuzo Araki ⁵ and Kohei Hamada ⁶

¹ Graduate School of Maritime Sciences, Kobe University, 5-1-1 Fukae-minami, Higashinada-Ku, Kobe 658-0022, Japan; ohsawa@port.kobe-u.ac.jp (T.O.)

² RWE Renewables Japan G.K., Marunouchi Trust Tower Main, 1-8-3 Marunouchi, Chiyoda-Ku, Tokyo 100-0005, Japan

³ International Meteorological & Oceanographic Consultants Co., Ltd., 9-9 Tsukiji 3-chome, Chuo-Ku, Tokyo 104-0045, Japan; asou@imoc.co.jp

⁴ Rera Tech Inc., 5-1-1 Fukae-minami, Higashinada-Ku, Kobe 658-0022, Japan; m.konagaya@rera-tech.co.jp (M.K.); t.misaki@rera-tech.co.jp (T.M.)

⁵ Japan Meteorological Corporation, Grand Front Osaka Tower-A 29F, 4-20 Ofukacho, Kita-Ku, Osaka 530-0011, Japan; araki@n-kishou.co.jp

⁶ E&E Solutions Inc., Akihabara UDX Building, 14-1 Sotokanda 4-chome, Chiyoda-Ku, Tokyo 101-0021, Japan; k-hamada@eesol.co.jp

* Correspondence: 171w304w@stu.kobe-u.ac.jp; Tel.: +81-80-4017-0637

Abstract: Floating LiDAR systems (FLSs) may replace conventional offshore met masts, and they have been developed well in Europe. However, before using them in Japan, we must determine whether they demonstrate the same performance under the unique East-Asian meteorological and oceanographic conditions. Therefore, herein, we investigate the performance of FLSs by focusing on the differences among models. Four independent wind datasets from three FLSs were simultaneously verified against a reference met mast and vertical LiDAR at a Japanese site. The data availability was confirmed to vary from 62.7 to 98.0% over the period at 63 m. This was strongly affected by the system availability of the buoy and LiDAR, suggesting that buoy system robustness is key to better campaigns with higher data availability. The 10 min averaged wind speed and direction largely satisfied the Carbon Trust's key performance indicators, with a low sensitivity to wave conditions depending on the buoy shape. The standard deviation of the wind speed and turbulence intensity had poorer accuracy than that of the 10 min averaged statistics because of the wave-induced buoy motion, especially for small buoys. In short, this paper provides an overview of a measurement by FLS in Japan. Also, the unique verification with multiple units suggests the need for a low-motion buoy or motion compensation to improve the measurement accuracy of the turbulence component.

Keywords: offshore measurement; floating LiDAR system; turbulence intensity; sensitivity analysis; motion compensation



Citation: Uchiyama, S.; Ohsawa, T.; Asou, H.; Konagaya, M.; Misaki, T.; Araki, R.; Hamada, K. Accuracy Verification of Multiple Floating LiDARs at the Mutsu-Ogawara Site. *Energies* **2024**, *17*, 3164. <https://doi.org/10.3390/en17133164>

Academic Editor: Andrey Starikovskiy

Received: 9 April 2024

Revised: 8 June 2024

Accepted: 13 June 2024

Published: 27 June 2024



Copyright: © 2024 by the authors. Licensee MDPI, Basel, Switzerland. This article is an open access article distributed under the terms and conditions of the Creative Commons Attribution (CC BY) license (<https://creativecommons.org/licenses/by/4.0/>).

1. Introduction

Floating LiDAR (light detection and ranging) systems (hereinafter referred to as FLSs) have been developed and have attracted considerable attention over the last decade as an alternative reliable wind measurement technology that may replace conventional offshore met masts [1–8]. The observation system is equipped with one or more units of vertical Doppler LiDAR and other meteorological and oceanological sensors on its floating buoy. Considering the wind industry's direction—e.g., having a larger turbine with a higher tower, shallow to deep water, and fixed to floating foundation—the FLS may be the only solution that can enable a trustworthy wind condition measurement at a height of up to 200 m or greater. In contrast, the offshore met mast no longer plays a major role in the measurement because the construction of a large offshore met mast at a site of interest is

technically and commercially infeasible owing to site constraints. In 2013, a roadmap for the commercial use of FLSs was released from the Offshore Wind Accelerator (hereinafter referred to as OWA) by the Carbon Trust (<https://www.carbontrust.com>, accessed on 12 June 2024), followed by version two of the roadmap in 2018 [9], wherein the development roadmap and key performance indicators (KPIs) for system robustness and measurement accuracy were defined.

Many studies on FLSs have thus been conducted, revealing their capability for enabling wind measurement. Owing to the nature of the measurement, the buoy and LiDAR are always affected by ocean conditions with translational and rotational motions. However, previous studies have shown a somewhat successful estimation of the 10 min averaged wind speed and direction, despite the raw wind measurement being contaminated by the aforementioned motions [1,10,11]. The measurement of the turbulence intensity (TI) is another important topic of discussion, in addition to the measurement of the averaged fields, as it is necessary for the turbine and foundation design. For some countries, including Japan, the project site for fixed-bottom offshore wind is limited to very nearshore areas owing to the steep increase in the water depth with the distance from the shore. For such nearshore projects, wherein the turbulent component is mainly generated by both the complex terrain and the thermal instability around the coastline, understanding the TI is more important. Several studies have discussed the measurement of the turbulence component using the FLS and suggested the need for a motion compensation algorithm to remove measurement errors due to additional motion caused by waves [1,12–15].

Although many studies have been conducted on the FLS to investigate its potential in wind measurement, few experimental results or publicly available verification results have been obtained in Japan or other Asia-Pacific regions, where the metocean conditions are expected to differ from those observed in European waters. The OWA roadmap explicitly notes that different tendencies in terms of the FLS accuracy may be observed if the test site has a metocean condition different from that of the previous verification trials conducted in Northern Europe, which used to be the main area in which FLS was studied [9]. In addition, previous research has rarely presented a comparison of multiple FLSs because the main discussion has been about the performance verification of one FLS unit against a reference offshore met mast or fixed vertical LiDAR (VL). Under these circumstances, the New Energy and Industrial Technology Development Organization (NEDO), a Japanese governmental body, conducted an experimental trial of offshore wind measurement technologies, including the FLS, at the Mutsu-Ogawara site on the east coast of Aomori Prefecture, to deepen the understanding of the measurement characteristics in Japan [16]. As part of this project, this study was conducted with the aim of investigating the comprehensive performance of three FLS units and four independent series of wind data, along with the KPIs proposed in the OWA roadmap. In addition, the turbulence measurement capabilities of the FLSs were investigated.

This is the first trial in which four concurrent and mostly full-year FLS measurements have been used along with reference wind data in Japanese coastal waters. This paper offers potential users of the FLS technology in Japan an overview of its expected performance and guidance on what needs to be taken care of. Aside from that, the comprehensive verification of a total of four units enables us to see the FLS performance from a different point of view, for example, the impact of having a different buoy shape. This will help the development of the FLS technology in general.

Following this section, Section 2 describes the multiple data sources used, provides a summary of the general metocean conditions observed at the site, and sets out the evaluation criteria. Section 3 explains the key findings, and Section 4 presents a discussion of them. Finally, Section 5 presents the conclusions of this study.

2. Data and Methods

2.1. Mutsu-Ogawara Site

The Mutsu-Ogawara Port observatory site is located on the east coast of Aomori Prefecture, in northeastern Japan, facing the Pacific Ocean. Three measurement stations are established: Onshore Station A1 (hereafter St. A1), having a 60 m tall met mast and multiple scanning and VLs; Onshore Station A2 (hereafter, St. A2), primarily for scanning LiDARs; and Station B (hereafter, St. B) having a 60 m tall met mast and a VL on a breakwater, which were treated as offshore measurements in this study. Three FLSs are deployed within a radius of 500 m from St. B. In addition, an ultrasonic wave height meter (NOWPHAS, Nationwide Ocean Wave Information Network for Ports and Harbors) is installed 1.5 km offshore from St. B [17]. The NOWPHAS data are used as a reference for the ambient wave height and period measurements. Figure 1 presents the locations of the Mutsu-Ogawara site and measurement facilities, and Figure 2 presents an aerial photograph. Because this study is focused on the performance verification of the FLS measurements, data from St. B and the FLS are primarily used. The detailed site conditions are discussed in previous research [18].

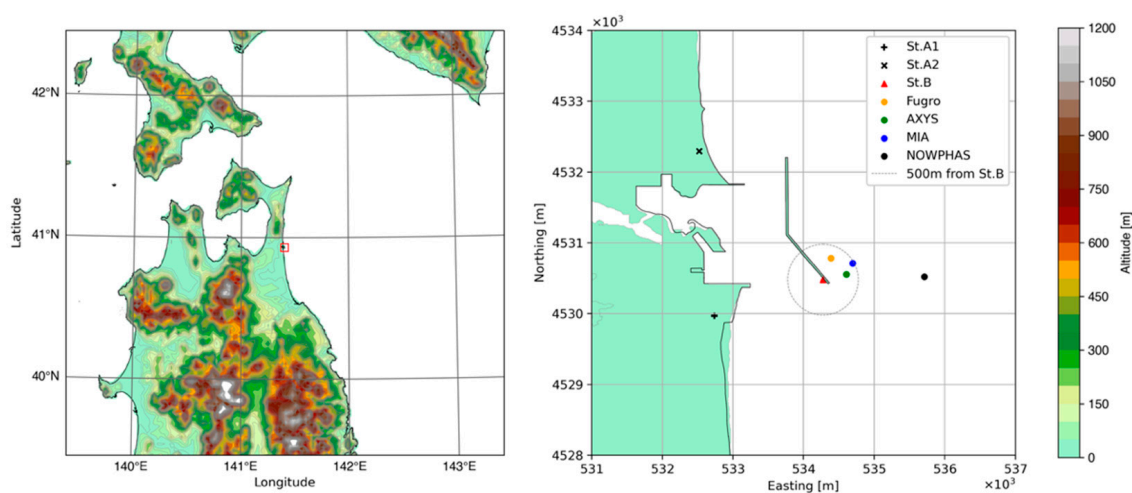


Figure 1. Locations of the Mutsu-Ogawara site and measurement facilities (the red rectangle on the left map shows the area of the right map).

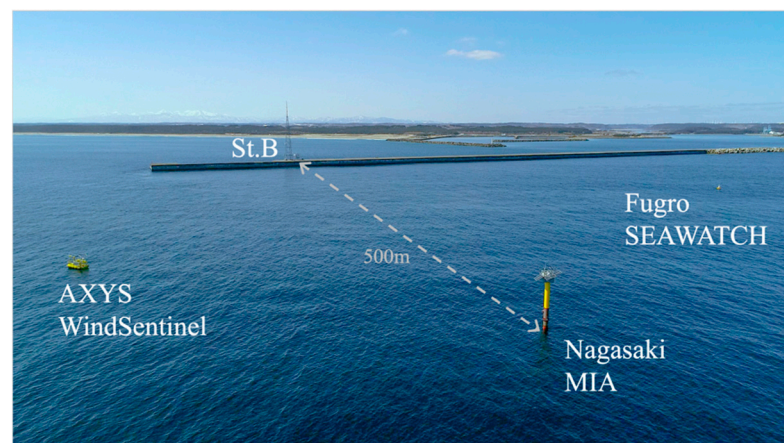


Figure 2. Aerial photo taken from the east side of the site.

2.2. Reference Met Mast and VL on the Breakwater

Figure 3 and Table 1 present the appearance and configuration of the met mast on the breakwater, respectively. It is an approximately 60 m tall self-standing met mast from the upper surface of the breakwater, which is 5 m above the mean sea level (AMSL); thus, the

top of the met mast is approximately 65 m AMSL. For convenience, all the altitudes are presented as AMSL in this study. The structure of the met mast is divided into two parts, a monopole above 50 m and a truss below 50 m, to minimize the effect of the structure of the met mast on the primary anemometers and vane. This study uses wind speed data merged from two three-cup anemometers mounted on 140–320° booms at 63 m for quality control. Data from the sensor on the side of the wind-direction semicircle are selected, i.e., the anemometer on the 140° boom is used for the wind direction from 50° to 230°, and the anemometer on the 320° side is used for the remaining wind directions. Moreover, to filter out outliers in each sensor, the 3σ rule is applied, such that the data do not include timestamps when the difference in the 10 min averaged wind speed between the two sensors is greater than 3σ of the difference for the whole measurement period. The merged data are also visually verified and confirmed to be quality controlled. This study uses the wind direction data from the vane on a 50° boom at 61 m. For the wind direction, special treatments, such as filtering for outliers or directional restriction for the mast shadow, are not considered because a few large differences are observed in the 10 min averaged wind direction compared to the sonic anemometer on the 50° boom at the same height.

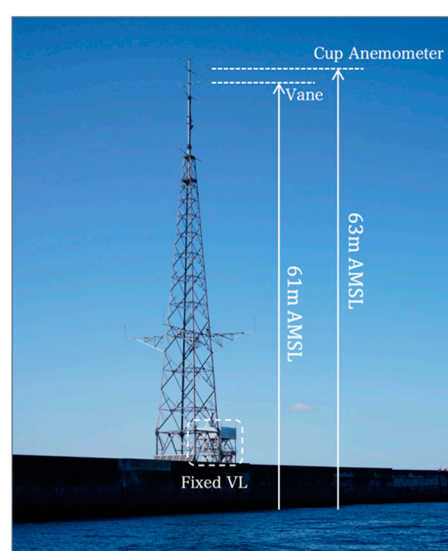


Figure 3. Appearance of the met mast and fixed VL of St. B.

Table 1. Measurements of the St. B met mast used in this study.

Period	From 24 November 2020 to 23 November 2021
Location	On breakwater in Mutsu-Ogawara Port, Aomori Prefecture
Structure	Self-standing truss + tubular, up to 65 m in height
Main sensors	63 m: three-cup anemometers (140° and 320° booms, NRG Systems Class 1) 61 m: Vane (50° boom, NRG Systems 200M) Sampling frequency: 1 Hz

Windcube V2.1 (a pulsed VL, hereinafter referred to as fixed-VL) is installed on the observation platform next to the met mast on the breakwater and configured to measure the wind speed and direction at several predefined representative heights, including 63 m, 120 m, and 180 m (Table 2). Because the difference between FLS and fixed-VL is only whether it is floating or fixed or whether the measurement is affected by its buoy motion, the data obtained from the fixed-VL are useful for understanding the effect of the FLS motion on the wind measurement accuracy, especially in the case of turbulent components. Therefore, the standard deviation of the wind speed (SD) and TI measured at 63 m using the fixed-VL are used as reference data, in addition to those from the primary three-cup

anemometer. Table 3 lists the data availability of the quality-controlled wind speed and direction from the met mast and VL for the verification period of 1 year, which is set from 24 November 2020 to 23 November 2021.

Table 2. Configuration of the VL at St. B.

Period	From 24 December 2020 to 23 November 2021
Location	On the observation platform next to the St. B met mast
LiDAR type	Windcube V2.1 (Vaisala, formerly Leosphere)
Measurement heights	50, 59, 63, 66, 80, 100, 120, 140, 160, 180, 200, and 250 m
Measurement parameters to be used	SD and TI at 63 m

Table 3. Data availability of the St. B met mast and fixed VL (wind speed and direction combined data at 63 m) [%]. (The values in italics represent the values calculated from non-full-month).

Year	2020		2021											All
Month	Nov	Dec	Jan	Feb	Mar	Apr	May	Jun	Jul	Aug	Sep	Oct	Nov	
Met mast	<i>100.0</i>	53.8	99.1	99.7	96.3	98.6	99.8	99.6	99.2	65.4	98.6	95.2	96.5	91.8
Fixed VL	-	66.2	99.8	99.9	99.9	99.9	96.7	100.0	99.8	69.7	99.5	99.9	94.3	91.9

2.3. Reference Wave Data

As shown in Figure 1, the NOWPHAS sensor is installed approximately 3 km from the coastline. The measurement is obtained using a seabed-type wave height gauge, and ultrasonic waves are used to capture the sea-surface fluctuations. Based on the zero-up crossing method, the NOWPHAS sensor obtains a significant wave height $H_{1/3}$ and period $T_{1/3}$, which represent the average of the highest third of the wave and its corresponding wave period, respectively.

2.4. Floating LiDAR System Used for the Research

Table 4 lists the three FLSs used in this study. The SEAWATCH Wind LiDAR Buoy manufactured by Fugro (headquartered in Leidschendam, The Netherlands) is a round buoy with single-point mooring and is equipped with a ZX300M by ZX Lidars (headquartered in Malvern, UK), a continuous-wave Doppler LiDAR (hereinafter referred to as FZX). WindSentinel, manufactured by AXYS Technologies (headquartered in Sidney, BC, Canada), is a ship-shaped buoy with a single-point mooring, which is similar to Fugro SEAWATCH but equipped with two types of LiDAR, ZX300M and Windcube (WSL866) by Vaisala (headquartered in Vantaa, Finland), which are referred to as AZX and AWC, respectively. This study treats these two data as independent datasets. It should be noted that the aforementioned SEAWATCH and WindSentinel are classified as “commercial” in accordance with the OWA roadmap and are widely used for actual offshore wind projects. The Marine Environmental Data Integrated Acquisition platform (MIA), jointly manufactured by five companies in Nagasaki Prefecture, Japan, is a spar-type buoy with three-point moorings and is considered to have low motion owing to its structural stability. DIABREZZA, a pulsed Doppler LiDAR by Mitsubishi Electric (headquartered in Tokyo, Japan), is mounted on the upper deck of the buoy (hereinafter referred to as MDB). As a motion compensation function is implemented in DIABREZZA, the data to be used for verification are already considered to be motion-compensated. Correction of the wind direction due to yaw motion within 10 min is enabled in all four LiDARs mounted on the three FLSs. However, the wind speed and TI corrections using a gyro sensor are only available for AWC and MDB.

A summary of the verification heights, including the reference measurements, is presented in Table 5. The period of verification is 12 months, from 24 November 2020 to 23 November 2021. The availability of FLS data is discussed in the next section as part of the verification results.

Table 4. Specifications of the FLSs.




	SEAWATCH	WindSentinel	MIA
Image			
Manufacturer	Fugro	AXYS Technologies	Nagasaki 5 companies
Shape	Round	Ship	Spar
Dimensions	Height: 7.2 m Diameter: Ø 2.8 m	Height: 9 m Length: 6 m Width: 3.1 m	Height: 26 m Diameter: Ø 1.0 m (above water level), Ø 2.15 m (below water level) Maximum platform width: 5.5 m
Weight	Approximately 2.2 tons	Approximately 9 tons	Approximately 46 tons Platform: 2 tons Floater: 44 tons
Draft	Approximately 3 m	Approximately 2 m	Approximately 14.5 m
Material	Polyethylene, aluminum, and copper	Aluminum and copper	Copper and concrete
Mooring	Single-point catenary with a mid-float	Single point catenary	3-point catenary
Drifting radius	Approximately 100 m	Approximately 120 m	Approximately 20 m
Mooring chain length	Approximately 85 m	Approximately 120 m	Approximately 320 m × 3 chains
LiDAR(s)	FZX: ZX300M (ZX Lidars)	AZX: ZX300M (ZX Lidars) AWC: Windcube (Vaisala)	MDB: DIABREZZA (Mitsubishi Electric)
Power	Fuel cell, photovoltaic (PV), and battery	Wind turbine, PV, battery, and diesel generator	Fuel cell, PV, and battery
Met. Parameters	Wind, temperature, and humidity	Wind, temperature, humidity, pressure, precipitation, and irradiance	Wind, temperature, humidity, and irradiance
Ocean parameters	Sea temperature, wave, and current	Sea temperature, wave, and current	Sea temperature

Table 5. Summary of the measurement heights (heights highlighted in blue are representative heights used for the analysis).

Height [m MSL]	Measurement					
	St. B Met Mast	St. B VL	FZX	AZX	AWC	MDB
250		○			○	Every 5 m up to 249 m
220					○	
200		○			○	
180		○	○	○	○	○ (179 m)
160		○			○	Every 5 m
140		○			○	

Table 5. Cont.

Height [m MSL]	Measurement					
	St. B Met Mast	St. B VL	FZX	AZX	AWC	MDB
120		○	○	○	○	○ (119 m)
100 or 102		○ (100 m)	○ (100 m)	○ (102 m)	○ (100 m)	
80		○			○	Every 5 m
66		○				
61, 63 or 64	Cup (63 m) Vane and sonic (61 m)	○ (63 m)	○	○	○	○ (64 m)
59	Cup/Propeller	○				Every 5 m from 54 m
50	Cup/Vane	○			○	
40 or 42			○ (40 m)	○ (40 m)	○ (42 m)	
25	Cup		○	○		
12			○	○		

2.5. Key Performance Indicators and Other Evaluation Criteria

This study primarily uses the key performance indicators (KPIs) proposed in the OWA for the verification of the wind speed and direction measured using the FLSs. Table 6 lists the KPIs for the system and data availability, and Table 7 lists the accuracy of the wind speed and direction measurements. For the wind speed, the bias defined by Equation (1) is also used to understand the systematic error in the measurement.

$$\text{Bias [\%]} = \frac{\overline{V_{FLS}} - \overline{V_{Ref}}}{\overline{V_{Ref}}} \times 100 \quad (1)$$

where V_{FLS} is the wind speed measured by the FLS, V_{Ref} is the reference wind speed, and $\overline{V_{Ref}}$ is the reference wind speed averaged over a period. Because no KPI has been proposed in the OWA with respect to the TI, this study has neglected the quantitative evaluation and instead qualitatively compares the FLS-measured TI with those measured using the three-cup anemometer and VL.

Table 6. KPIs for availability.

Type	Description	Acceptance Criteria	
		Stage 3	Stage 2
MSA _{1M}	Monthly system availability	≥90%	≥85%
MPDA _{1M}	Monthly post-processed data availability	≥85%	≥80%

Table 7. KPIs and other evaluation criteria for accuracy.

Parameter	Condition	Type	Description	Acceptance Criteria	
				Best Practice	Minimum
Wind speed	≥2 m/s and 4–16 m/s	Slope (X_{mws})	Slope of single variant regression	0.98–1.02	0.97–1.03
		R^2 (R^2_{mws})	Coefficient of determination from single variant regression	>0.98	>0.97
		Bias (B_{mws})	Relative mean error	Not defined	
Wind direction	≥2 m/s	Slope (M_{mwd})	Slope of two-variant regression	0.97–1.03	0.95–1.05
		Offset (OFF_{mwd})	Offset of two-variant regression	<5°	<10°
		R^2 (R^2_{mwd})	Coefficient of determination from two-variant regression	>0.97	>0.95

3. Results

3.1. Metocean Conditions during the Verification

It is worth noting that the site is located near the shore; thus, a horizontal speeding up in the shore-normal direction should be carefully considered and treated in the verification, especially for wind blowing from land to sea (hereinafter referred to as the land sector) owing to the change in the onshore and offshore surface roughness. A pre-assessment revealed the wind speed difference from the St. B met mast to the FLS locations could reach approximately 3% for the land sector. This 3% difference is critical in this study for validating the FLS-measured wind speed because the horizontal separation of the FLSs from the reference mast is ideally required to be taken into consideration to avoid a misinterpretation of the verification result. Therefore, this study is simply focused on only the wind blowing from the Pacific Ocean side, ranging from 0° to 180° (hereinafter referred to as the sea sector), which is often observed in spring to summer and accounts for up to 40% throughout the year at the site.

Figure 4 presents the wind distribution and wind rose during the verification period. The observed average wind speed for the sea sector is 7.92 m/s. The observed TI is presented in Figure 5. From the figure, the turbulence is confirmed to be similar to that observed at a typical offshore project site [19], where the 90-percentile line is below the line of the International Electrotechnical Commission (IEC)'s normal turbulence model category C.

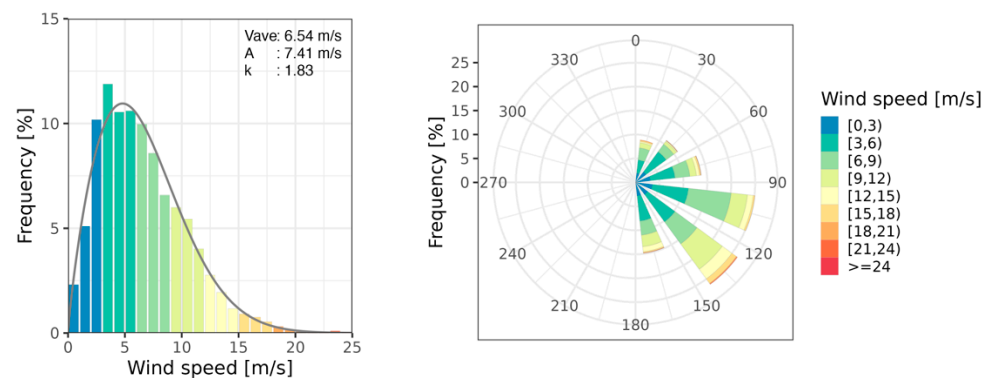


Figure 4. Wind distribution, averaged wind speed and Weibull parameters A and k (left) and wind rose (right) based on the anemometer at 63 m combined with the vane at 61 m during the verification period—sea sector only.

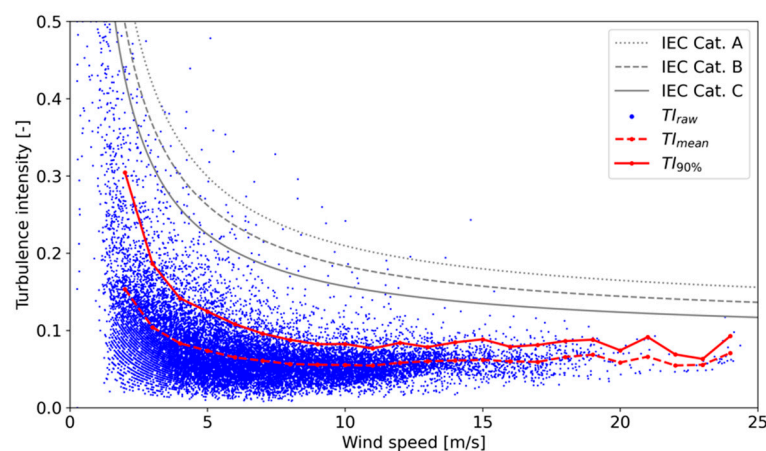


Figure 5. Ambient TI at 63 m as a function of wind speed—sea sector only. The blue plots represent raw samples of the TI, while the red line indicates the 90-percentile values in every 1 m/s binned wind speed. The IEC's normal turbulence model is also shown.

A heat map of the observed significant wave heights and periods is presented in Figure 6. The significant wave period varies from approximately 4 to 12 s, with a peak at approximately 7.0 s and an average value of 7.2 s. The swell component, which is often found on the side of the Pacific Ocean, contributes to the relatively large wave period at the site. The significant wave height varies from approximately 0.3 to 3.7 m, with a peak at approximately 1.0 m and an averaged value of 1.3 m.

The requirement of the number of samples is verified using filtering based on the aforementioned wind direction. Table 8 lists the number of samples in each wind speed bin defined in the OWA roadmap. All the units are confirmed to satisfy the requirement, which is set as 40 samples in each 1 m/s width bin ranging from 2.0 to 12.0 m/s and 2 m/s width bin from 12.0 to 16.0 m/s. The difference in the samples between the FLS units and the corresponding reason is discussed in a later section.

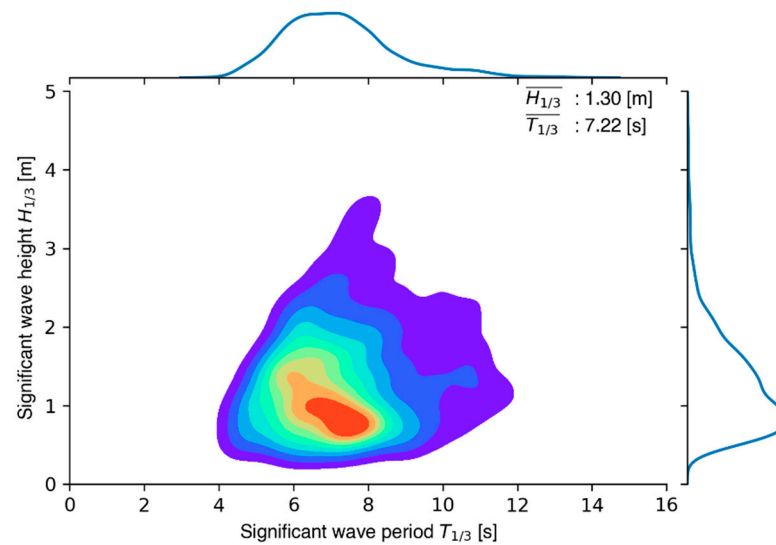


Figure 6. Ambient wave condition—sea sector only. The x and y axes represent a significant wave period and height, respectively.

Table 8. Number of samples in each bin for all four units—sea sector only (the rows highlighted in blue indicate the wind speed bins required to contain more than 40 samples).

Bin [m/s]	Range [m/s]		Samples [-]			
	Start	End	FZX	AZX	AWC	MDB
−2.0	0.0	2.0	727	673	1387	1003
2.5	2.0	3.0	1163	989	1906	1454
3.5	3.0	4.0	1324	1214	2219	1667
4.5	4.0	5.0	1152	1030	1960	1588
5.5	5.0	6.0	1244	1034	1946	1644
6.5	6.0	7.0	1199	968	1820	1613
7.5	7.0	8.0	929	681	1582	1485
8.5	8.0	9.0	699	489	1230	1104
9.5	9.0	10.0	576	399	1121	1006
10.5	10.0	11.0	409	316	1019	957
11.5	11.0	12.0	308	286	753	690
13.0	12.0	14.0	365	425	883	789
15.0	14.0	16.0	167	257	389	337
16.0–	16.0	-	224	258	375	286
Total	-	-	10,486	9019	18,590	15,623

3.2. Analysis of the Buoy Motion

The accuracy of the FLS is expected to be sensitive to the buoy motion. Thus, the characteristics of each FLS buoy are discussed before verifying its accuracy. To quantify the motion, the buoy tilt θ_α is analyzed at every timestep using Equation (2), with the roll θ_r and pitch θ_p recorded using a gyro sensor on the buoy.

$$\theta_\alpha = \cos^{-1}(\cos \theta_r \cos \theta_p) \quad (2)$$

Next, a significant tilt $\theta_{\alpha,1/3}$ is defined as shown in Equation (3) in a manner similar to the significant wave height, which is calculated as an average of the highest one-third of the wave heights accumulated within the averaging window.

$$\theta_{\alpha,1/3} = \frac{1}{\frac{1}{3}N} \sum_{m=1}^{\frac{1}{3}N} \theta_{\alpha,m} \quad (3)$$

Here, N is the number of peaks within the window, which is set as 10 min, and $\theta_{\alpha,m}$ is the individual maximal value of the buoy tilt sorted into the descending order. $\theta_{\alpha,1/3}$ indicates how large the buoy motion is. This is assessed along with the peak period of the roll and pitch of the buoy. Figure 7 presents the results of the significant tilt and peak periods for the three buoys. It is interesting to note that the motion of a buoy varies widely depending on its type. In terms of the significant tilt, the SEAWATCH buoy exhibits the greatest motion, MIA exhibits the least motion, and WindSentinel exhibits the median motion. In the case of the peak period, SEAWATCH and WindSentinel exhibit smaller values (up to 5 s), while MIA presents a very different distribution, with a peak at approximately 20 s. WindSentinel has different peak periods for roll and pitch, probably owing to its anisotropic shape. Irrespective of the different peaks, the variation in the peak period is much smaller than that of the significant tile, suggesting that the period of the buoy motion does not correlate with the variable wave period. From this analysis, it is apparent that, compared to SEAWATCH and WindSentinel, the MIA buoy is significantly more stable thanks to its spar shape.

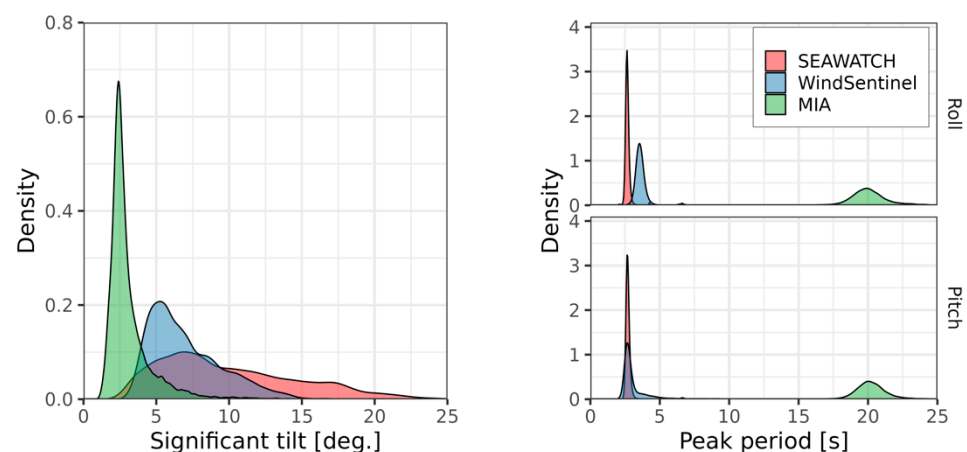


Figure 7. Frequency distributions of the FLS buoys' significant tilt (**left**) and peak period (**right**).

3.3. System and Data Availability

Tables 9–12 summarize the monthly and overall system and data availability for FZX, AZX, AWC, and MDB, respectively. The system availability is calculated based on the number of recorded timestamps in the existing data, and the main factors for the parameter would thus comprise the stable buoy system, the power supply to the LiDAR on it, and the health of the LiDAR. It should be noted that a buoy system that cannot store and/or deliver the measured data—for example, because of an interface problem between the LiDAR unit and the buoy system or a poor Internet connection—results in a lower system

availability. For data availability, this study is focused on predefined representative heights of approximately 63 m, 120 m, and 180 m. The tables also present the data availability relative to the system availability, which is considered to be solely dependent on the LiDAR unit. The main factor affecting the decrease in this data availability would be environmental parameters such as the visibility.

Table 9. System and data availability for FZX (the values in italics represent the values calculated from non-full-month data and the values in parentheses indicate the data availability relative to the system availability).

2020–2021	System Availability [%]	Data Availability (Relative to System Availability) [%]		
		63 m	120 m	180 m
November	100.0	99.0 (99.0)	98.9 (98.9)	98.9 (98.9)
December	100.0	99.3 (99.3)	99.2 (99.2)	99.0 (99.1)
January	100.0	99.3 (99.3)	99.1 (99.1)	98.7 (98.7)
February	100.0	99.7 (99.7)	98.9 (98.9)	98.3 (98.3)
March	100.0	99.7 (99.7)	98.9 (98.9)	97.5 (97.5)
April	43.6	43.1 (98.8)	43.2 (98.9)	42.9 (98.4)
May	100.0	98.9 (98.9)	97.1 (97.1)	95.5 (95.5)
June	100.0	96.4 (96.4)	91.0 (91.0)	88.2 (88.2)
July	78.9	71.6 (90.7)	61.6 (78.1)	58.4 (74.0)
August	0.0	0.0 (-)	0.0 (-)	0.0 (-)
September		No measurement		
October				
November				
Overall	80.6	79.0 (98.0)	76.9 (95.4)	75.8 (94.0)

Table 10. Same as Table 9 but for AZX.

2020–2021	System Availability [%]	Data Availability (Relative to System Availability) [%]		
		63 m	120 m	180 m
November	99.8	98.0 (98.2)	97.7 (97.9)	97.6 (97.8)
December	99.8	98.5 (98.7)	93.4 (93.6)	89.9 (90.1)
January	99.9	97.7 (97.8)	92.1 (92.2)	87.5 (87.6)
February	99.8	92.8 (93.0)	87.7 (87.9)	83.6 (83.7)
March	77.3	77.2 (99.8)	75.2 (97.3)	73.8 (95.4)
April	96.2	95.8 (99.6)	93.2 (96.9)	90.2 (93.8)
May	97.9	96.3 (98.3)	91.9 (93.8)	88.7 (90.5)
June	74.4	70.1 (94.2)	65.6 (88.1)	62.9 (84.6)
July	28.5	27.0 (94.7)	22.2 (77.9)	20.6 (72.2)
August	0.0	0.0 (-)	0.0 (-)	0.0 (-)
September	0.0	0.0 (-)	0.0 (-)	0.0 (-)
October	16.7	16.4 (98.1)	14.8 (88.7)	14.1 (84.5)
November	82.2	78.8 (95.8)	77.5 (94.2)	75.8 (92.1)
Overall	64.5	62.7 (97.2)	59.6 (92.5)	57.5 (89.1)

Table 11. Same as Table 9 but for AWC.

2020–2021	System Availability [%]	Data Availability (Relative to System Availability) [%]		
		63 m	120 m	180 m
November	100.0	100.0 (100.0)	100.0 (100.0)	99.2 (99.2)
December	99.9	99.9 (100.0)	99.9 (100.0)	99.1 (99.1)
January	99.9	99.9 (100.0)	99.8 (100.0)	99.1 (99.3)
February	74.4	74.4 (100.0)	74.4 (100.0)	72.9 (97.9)
March	100.0	100.0 (100.0)	100.0 (100.0)	99.1 (99.1)
April	100.0	99.9 (99.9)	99.9 (99.9)	98.7 (98.7)
May	100.0	99.8 (99.8)	99.7 (99.8)	98.1 (98.1)
June	100.0	100.0 (100.0)	98.4 (98.4)	92.2 (92.2)
July	99.9	99.9 (100.0)	99.6 (99.7)	91.1 (91.2)
August	100.0	100.0 (100.0)	99.5 (99.5)	94.5 (94.5)
September	100.0	100.0 (100.0)	100.0 (100.0)	99.7 (99.8)
October	99.8	99.8 (100.0)	99.8 (100.0)	99.4 (99.6)
November	99.9	99.9 (100.0)	99.8 (99.9)	98.6 (98.7)
Overall	98.0	98.0 (100.0)	97.7 (99.8)	95.4 (97.3)

Table 12. Same as Table 9 but for MDB.

2020–2021	System Availability [%]	Data Availability (Relative to System Availability) [%]		
		64 m	119 m	179 m
November	100.0	99.8 (99.8)	98.4 (98.4)	92.8 (92.8)
December	96.5	96.2 (99.7)	95.6 (99.0)	90.6 (93.9)
January	35.1	35.1 (100.0)	34.7 (98.8)	33.8 (96.2)
February	83.5	82.9 (99.3)	81.7 (97.9)	77.9 (93.3)
March	69.9	69.7 (99.7)	69.4 (99.2)	67.4 (96.3)
April	86.9	86.2 (99.2)	85.4 (98.2)	80.5 (92.7)
May	29.4	28.9 (98.5)	28.6 (97.4)	27.0 (91.8)
June	68.3	68.3 (99.9)	64.7 (94.6)	55.8 (81.7)
July	99.9	97.5 (97.6)	92.5 (92.7)	73.6 (73.7)
August	99.9	99.4 (99.5)	95.9 (96.0)	85.6 (85.7)
September	99.9	99.5 (99.6)	98.3 (98.4)	94.7 (94.8)
October	100.0	99.2 (99.3)	97.2 (97.2)	90.5 (90.5)
November	95.7	95.5 (99.8)	92.7 (96.8)	84.6 (88.4)
Overall	80.4	79.8 (99.3)	78.0 (97.1)	71.9 (89.4)

In the case of the Fugro SEAWATCH buoy (Table 9), as it was washed out by a typhoon at the end of July 2021, after which there were no available data, the overall system and data availabilities are calculated based on the data for approximately 10 months (November 2020–August 2021). In addition to the washed-out accident, the buoy underwent onshore maintenance, including refueling in April 2021, which resulted in lower system and data availability. For the remaining months, the system and data availability scores were greater than the OWA KPI Stage 3 criteria. It is also found that the data availability decreases with

an increase in the measurement height owing to fog or low-level clouds in the summer season as well as the nature of the LiDAR measurement.

In the case of AZX (Table 10), relatively low system and data availabilities were recorded in March 2021 and from June to November 2021. Considering the availability of the AWC, which is described subsequently, the buoy system appears to have been running during these periods. This is most likely because the LiDAR was not operating. In the case of AWC (Table 12), satisfactorily higher system and data availabilities were recorded, except for February 2021, when it was found that the LiDAR was not operational.

The MDB (Table 13) exhibits intermittently low system and data availability during the campaign, particularly from January to June 2021. The reported cause was an issue in the functioning of the power system, which comprised a fuel cell battery, and the LiDAR unit thus lacked a power supply. From the results of the data availability relative to the system availability, it appears that the data availability for the Stage 3 KPI would be almost achievable if the system worked well throughout the campaign. The results of the campaign demonstrate to FLS users the importance of realizing robustness and redundancy in the buoy and LiDAR systems.

Table 13. Accuracy of wind speed measurement (results that satisfy the best practice are highlighted in green).

Type	Condition	FZX	AZX	AWC	MDB	Acceptance Criteria
Slope (X_{mws})	≥ 2 m/s	0.999	1.001	1.017	1.023	Best Practice: 0.98–1.02 Minimum: 0.97–1.03
	4–16 m/s	1.001	1.004	1.020	1.024	
R^2 (R^2_{mws})	≥ 2 m/s	0.991	0.992	0.993	0.990	Best Practice: >0.98 Minimum: >0.97
	4–16 m/s	0.985	0.987	0.989	0.985	
Bias (B_{mws}) [%]	≥ 2 m/s	0.0	0.3	1.7	2.3	Not defined
	4–16 m/s	0.1	0.4	2.0	2.4	

When comparing the data availability from the four units at different heights, it is worth noting the decrease in the availability with an increase in the height. To analyze this, the measured visibility collected until July 2021 by a transmissometer next to the St. B met mast is compared with the data availability at approximately 180 m relative to that at approximately 63 m. In Figure 8, a clear relationship can be observed between the decrease in the availability and visibility. For example, the data availability decreases in January and July 2021, when a visibility of less than 1000 m is observed more frequently than in other months. This is apparent for AZX, but not for AWC and FZX, which appear to have less sensitivity to visibility. In general, the more frequently low visibility occurs, the smaller the number of measurement samples obtained in 10 min. To understand the differences among the units, an additional analysis is conducted while focusing on the number of samples in 10 min and the ratio of valid to invalid judgements. The results of the measurement at 180 m are presented in Figure 9. The x -axis represents the number of samples in 10 min, which is calculated by dividing 600 s (10 min) by the sampling frequency for pulsed LiDARs (AWC and MDB) or by direct derivation from a record in the 10 min interval for continuous-wave LiDARs (FZX and AZX). The y -axis represents the occurrence of samples judged to be valid or invalid in each bin. From the figure, it is confirmed that FZX primarily uses 10 samples as the judgment threshold. In contrast, AZX and MDB do not appear to have a fixed threshold but determine the validity based not only on the number of samples but also on other factors, which could be environmental parameters or the occurrence of outliers. It is interesting to observe the loose threshold in AWC, which indicates that even if only one or two samples are collected in 10 min, they are used to generate valid data of the 10 min averaged wind speed and direction. This is probably why the AWC data availability is less sensitive to the visibility.

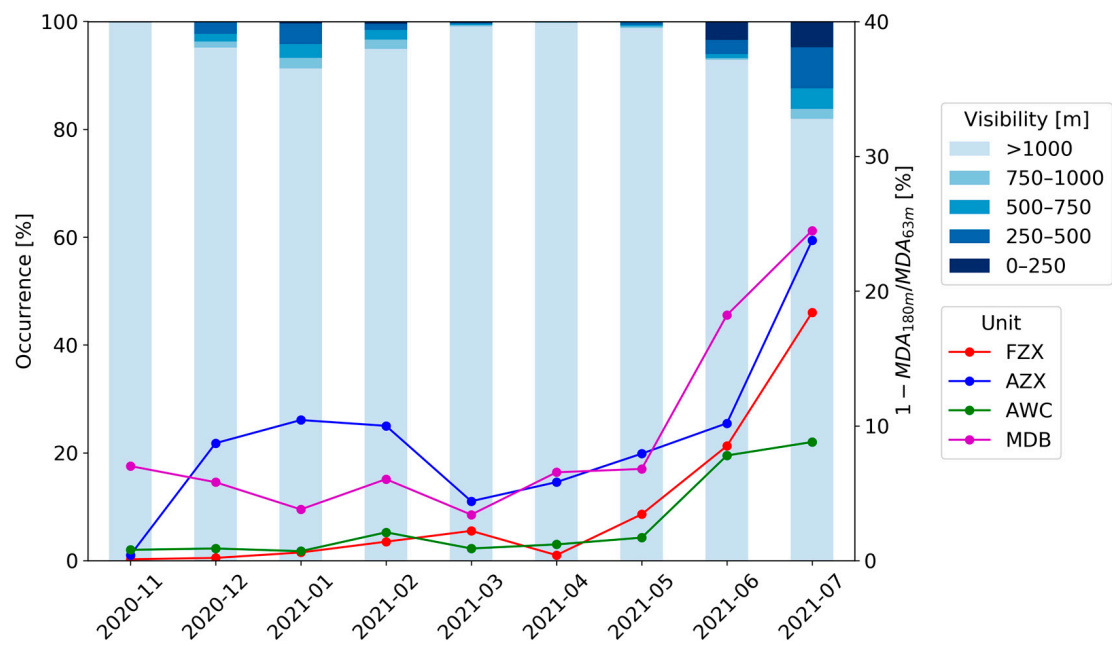


Figure 8. Monthly occurrence of visibility and data availability difference between 63 m and 180 m (the difference is shows as $(MDA_{63m} - MDA_{180m}) / MDA_{63m} \times 100$ [%]).

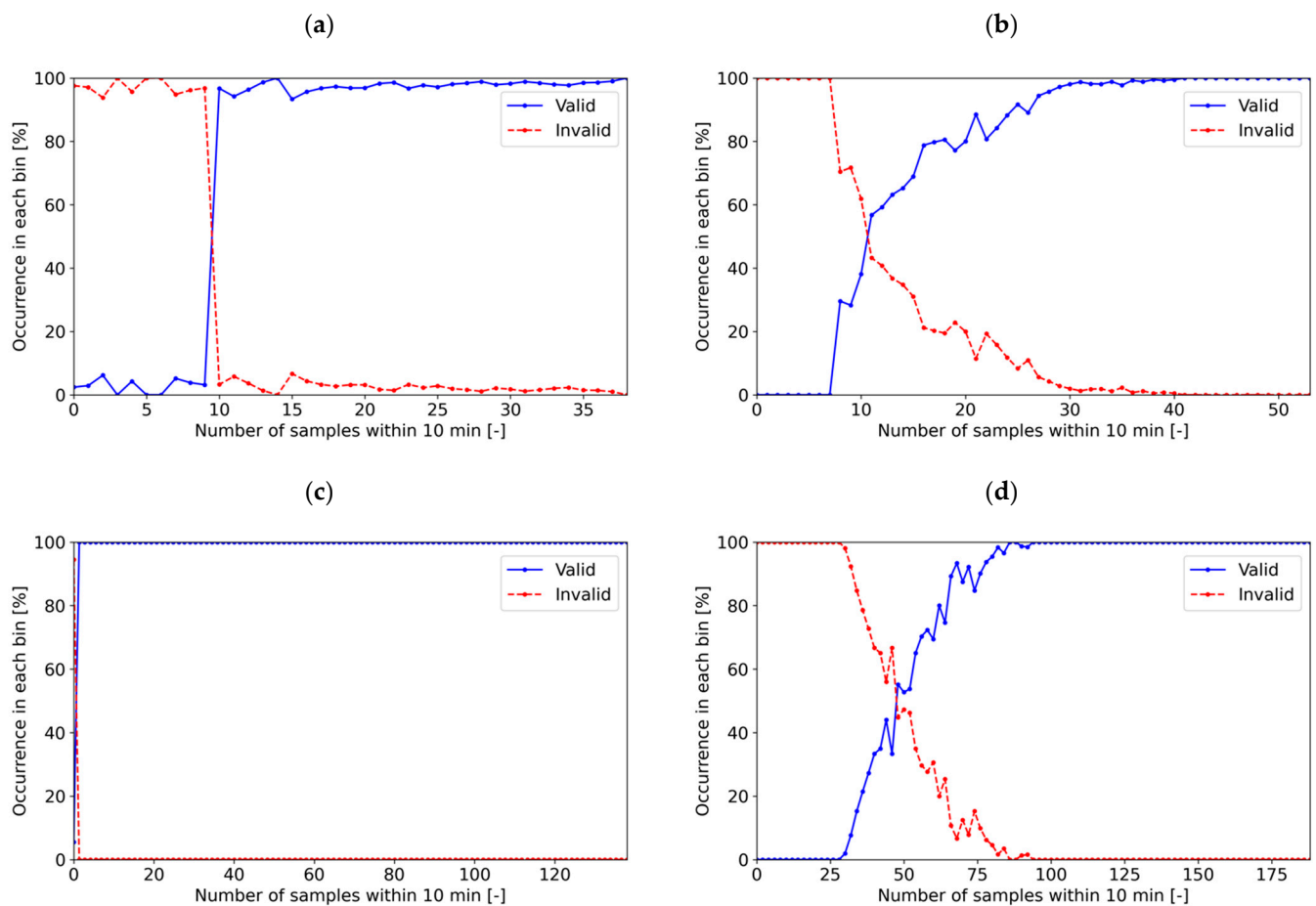


Figure 9. Relationship between the number of samples within a 10 min measurement window and judgement of the valid or invalid data at 180 m: (a) FZX, (b) AZX, (c) AWC, and (d) MDB.

3.4. Ten-Minute Averaged Wind Speed and Direction

Table 13 summarizes the accuracy of the FLS-measured wind speeds in accordance with the OWA KPIs. In the table, the cells highlighted in green indicate that the best practice requirements are met. From the slope of the single variant regression (X_{mws}), it is observed that FZX, AZX, and AWC satisfy the best practice, while MDB has a slightly larger slope and results in the “Minimum”. Similarly, a larger positive relative bias (B_{mws}) is observed for the MDB. However, caution must be exercised when interpreting these results and one cannot simply conclude that the MDB tends to overestimate the wind speeds. This is because a spatial separation of 500 m between the reference met mast at St. B and the MIA buoy can generate an unintentional gap in the wind speed (it should be noted that the buoy is located farther offshore than the met mast, as shown in Figure 1). With respect to the coefficient of determination for the regression (R^2_{mws}), all the units successfully satisfied the best practice. However, the R^2_{mws} for the wind speed ranging from 4 to 16 m/s tends to have slightly smaller values than those for wind speeds greater than 2 m/s. Figure 10 presents the scatter plots of the wind speeds obtained from the four units for wind speeds greater than 2 m/s. No notable differences between the units can be observed in the figure. The results suggest that, irrespective of the type of floater or LiDAR (and its measurement mechanism), the floating LiDAR system can return equally satisfactory results for the wind speed when viewed at this level of granularity.

Table 14 summarizes the accuracy of the FLS-measured wind direction with the OWA KPIs. Figure 11 presents the scatter plots of the wind direction from the four units against the reference mast measurements. It should be noted that a 180° flip, which is occasionally observed in the wind direction from ZX LiDAR (specifically FZX and AZX) owing to the nature of the measurement, has been corrected by the reference mast or the other concurrent measurement because the flip makes the result difficult to interpret. The correction of the flip using available concurrent data such as a met mast measurement or reanalysis dataset is recommended for actual use at a project site. For the slope of the two-variant regression (M_{mwd}), all the units exhibit values very close to 1 and satisfy the best practice. Similarly, R^2_{mwd} remains within the range of the best practice. However, the OFF_{mwd} value for MDB does not satisfy the best practice but remains within the minimum criteria. A problem was reported with the heading sensor in the MDB measurement, which seems to have caused a systematic error of approximately 6.2°. All the units are capable of satisfying the best practice in the measurement of the 10 min averaged wind speed and direction, even in Japanese coastal waters, at least on the Pacific Ocean side.

Table 14. Accuracy of the FLS-measured wind direction (results that satisfied the best practice are highlighted in green).

Type	Condition	FZX	AZX	AWC	MDB	Acceptance Criteria
Slope (M_{mwd})	≥ 2 m/s	0.998	0.996	0.998	0.996	Best Practice: 0.97–1.03 Minimum: 0.95–1.05
Offset (OFF_{mwd})		−0.405	0.320	−1.482	6.167	Best Practice: $<5^\circ$ Minimum: $<10^\circ$
R^2 (R^2_{mwd})		0.990	0.985	0.995	0.989	Best Practice: >0.97 Minimum: >0.95

To further investigate the accuracy of FLSs in measuring the wind speed with finer granularity, the sensitivities of the environmental conditions to their accuracy are verified, with a special focus on the wave height and period, which are considered key parameters that determine the accuracy characteristics of FLSs.

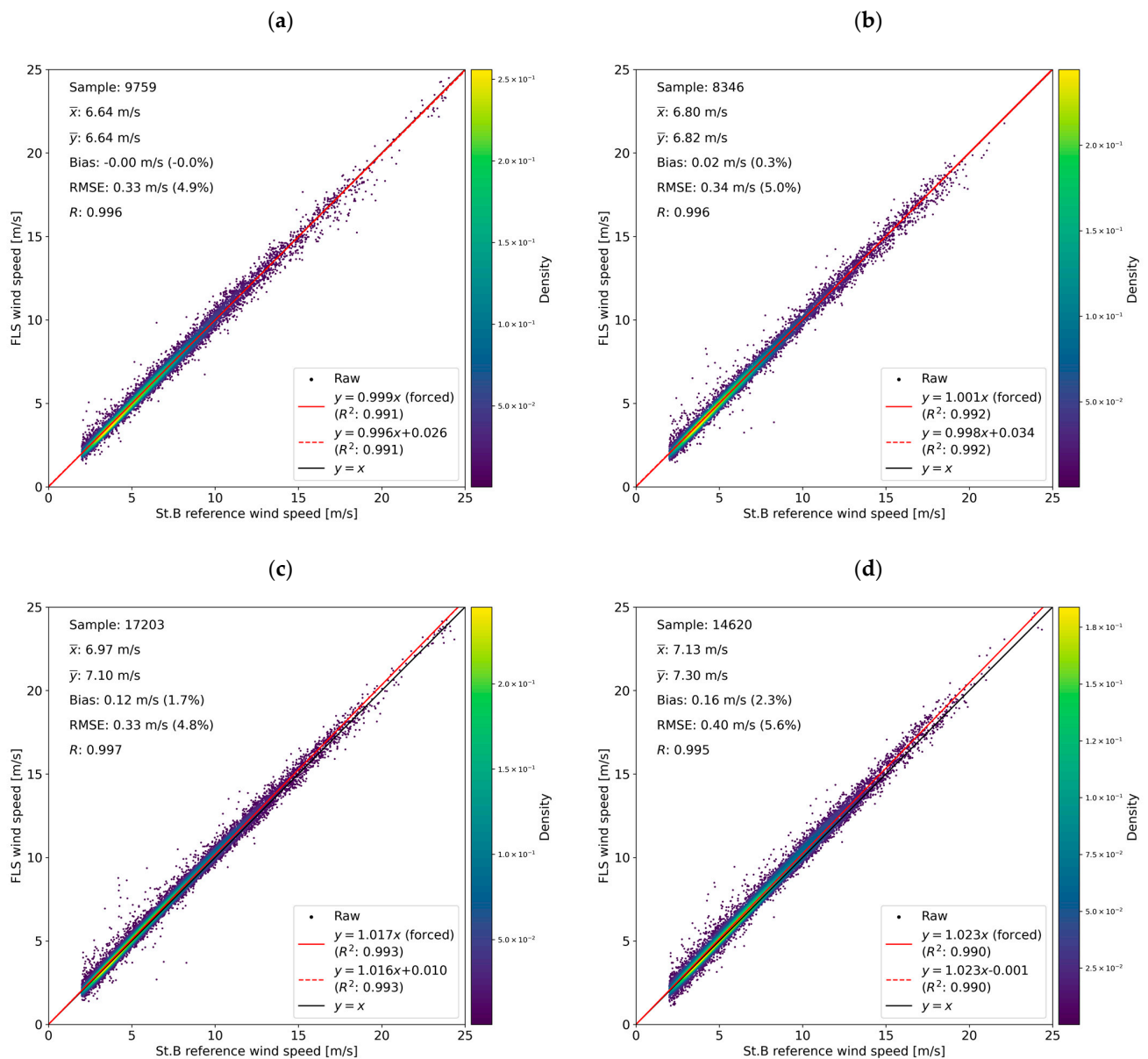


Figure 10. Scatter plots of the wind speeds from the reference met mast and FLSs for a 10 min wind speed range over 2 m/s: (a) FZX, (b) AZX, (c) AWC, and (d) MDB.

Figures 12 and 13 present the results of the sensitivity analysis of the accuracy of the FLS wind speed to the significant wave height and peak period, respectively. In both figures, the x -axis represents each environmental parameter, and the y -axis represents the deviation of the FLS wind speed relative to the cup wind speed. Both are based on the wind speed at 63 m. Two types of regression lines were obtained for the raw samples and the bin averages considered valid in terms of the number of samples (according to the IEC standard's classification study [20]), and the regression for the valid bin averages is discussed here. The sensitivity is evaluated based on the slope of the regression and the coefficient of determination (R^2). In Figure 12, the slope of the regression line has a positive value, and there is a positive correlation between the deviation and the significant wave height. This means that as the significant wave height increases, the FLS wind speed tends to be slightly overestimated. In addition, a cross-comparison among the units results in two interesting interpretations. Firstly, when AZX and AWC (two units on the same buoy) are compared, the continuous-wave LiDAR (AZX) appears to have less sensitivity to a significant wave height. Secondly, a comparison between the same types of LiDAR (i.e., FZX and AZX as a

continuous-wave LiDAR or AWC and MDB as a pulsed LiDAR) suggests that the sensitivity to a significant wave height is greater when measured using a small buoy with large motions. However, the difference is insufficiently significant for drawing a conclusion, and further investigation is required in several cases. Figure 13 shows that the FLS wind speed is less sensitive to the wave period. This result is expected because the period of the buoy's motion is almost independent of the wave period, as shown in Figure 7. However, some sensitivity may be derived from other environmental parameters that have some indirect correlation with the wave period via its seasonal trend, e.g., in terms of the wind speed and shear. Nonetheless, this can explain why the accuracy of the FLS measurement at the Mutsu-Ogawara site is not significantly different from that obtained in European seas (as shown in Section 3.4) despite the prevailing longer wave periods owing to the swell in the Pacific. However, with finer granularity, some FLS-measured wind speeds are sensitive to the sea states, especially for significant wave heights. This implies that there is room for further improvement in the FLS measurements, which can be realized by adopting more sophisticated motion compensation algorithms based on the wave conditions.

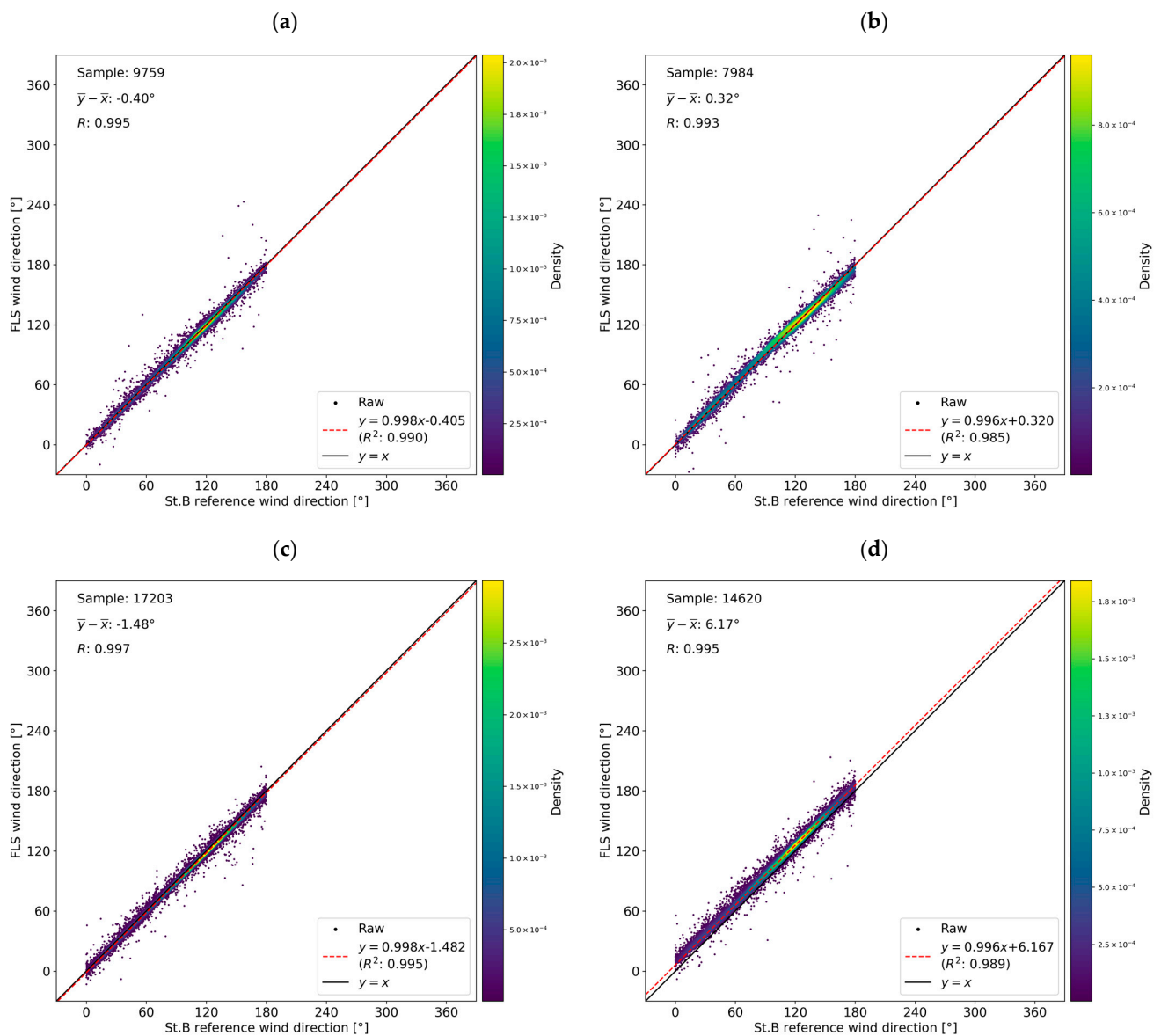


Figure 11. Scatter plots of the wind directions from the reference met mast and FLSs for a 10 min wind speed range above 2 m/s (as mentioned before, the analysis is limited to the sea sector from 0° to 180°): (a) FZX, (b) AZX, (c) AWC, and (d) MDB.

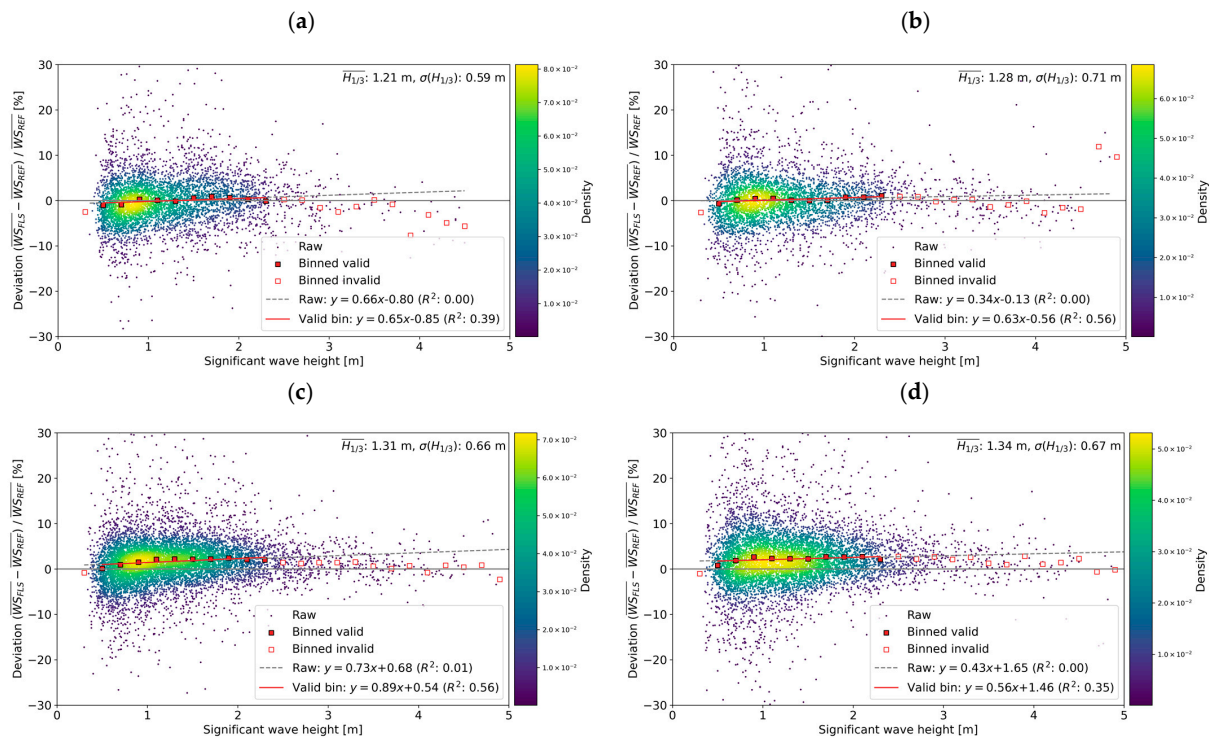


Figure 12. Sensitivity of the deviation of the FLS wind speed from the cup wind speed to a significant wave height Only the samples of the 10 min wind speed over 2 m/s are used. Deviation is expressed as a value relative to the cup wind speed. The rectangles indicate averages of the deviation for wind speed bins of a 0.2 m width, and valid values are indicated in red. The gray and red lines indicate regression lines for raw samples and valid bin averages, respectively. The average and standard deviation of the significant wave height are also presented in the figures. (a) FZX, (b) AZX, (c) AWC, and (d) MDB.

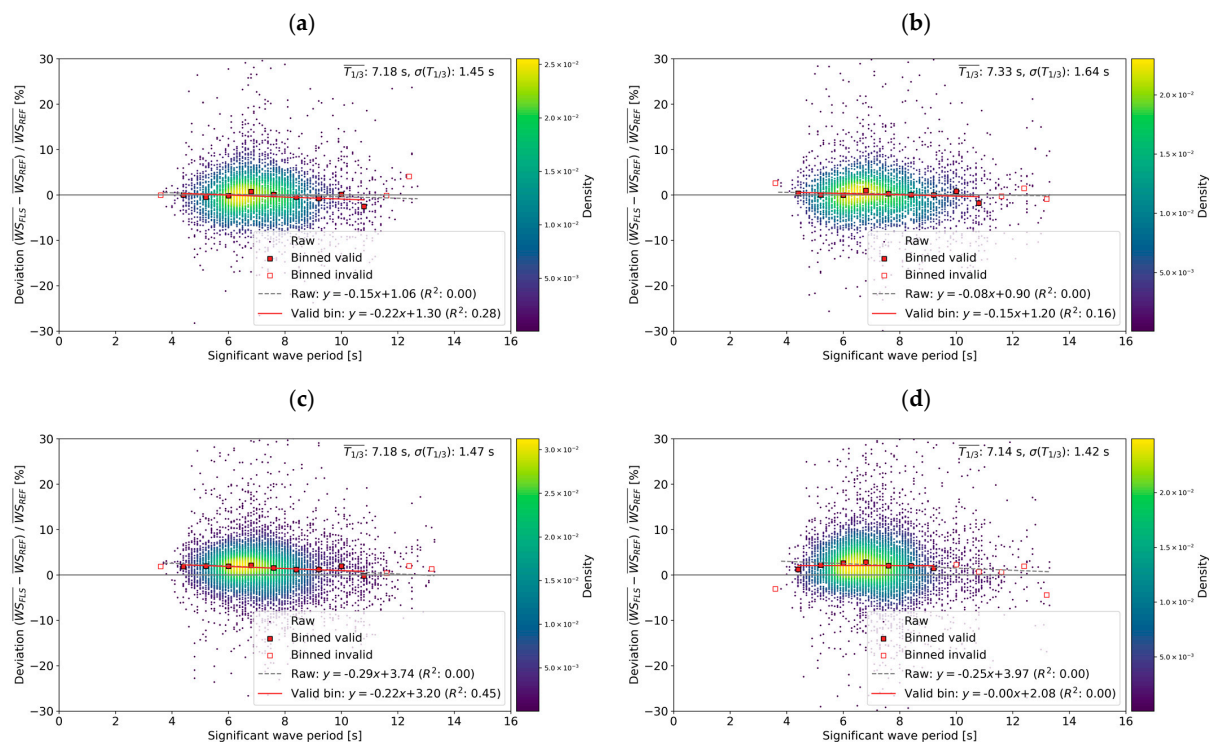


Figure 13. Same as Figure 12 but for the sensitivity to the peak period (bin width is set as 0.8 s): (a) FZX, (b) AZX, (c) AWC, and (d) MDB.

3.5. Ten-Minute Standard Deviation of Wind Speed and Turbulence Intensity

When discussing the capability of the FLS in terms of capturing the turbulence component, it is important to consider that the error derived from the FLS measurement can be categorized into two main factors. One factor is the buoy motion, which generates a false turbulence component in every raw measurement. This effect was confirmed to be almost negligible in the case of the 10 min averaged wind speed, as in the previous section, but it cannot be overlooked in the case of the SD. The other factor is the measurement principle of the VL, i.e., the volume measurement. The VL (irrespective of being mounted on an FLS or fixed platform) assumes homogeneity in the wind flow in the measurement volume and measures the wind speed as the volume average (in contrast to a conventional cup anemometer, which measures the wind speed at a point). Thus, the VL-measured turbulence is inherently different from that measured using a cup anemometer [21–24]. Therefore, the FLS-measured SD and TI must be verified against both the fixed VL and cup anemometers.

First, the SD from the fixed VL at St. B is compared with that from the cup anemometer as a reference. Figure 14 presents a scatter plot of the SDs from the cup and VL, wherein only the samples with wind speeds over 2 m/s are used. The bias of the VL against the cup is 0.06 m/s (12.6%), and the slope of the single variant regression is 1.105, while the R^2 remains relatively high (0.905). This implies that the SD from the fixed VL includes a systematic error owing to its measurement principle and tends to be slightly overestimated. This is consistent with the results of previous studies.

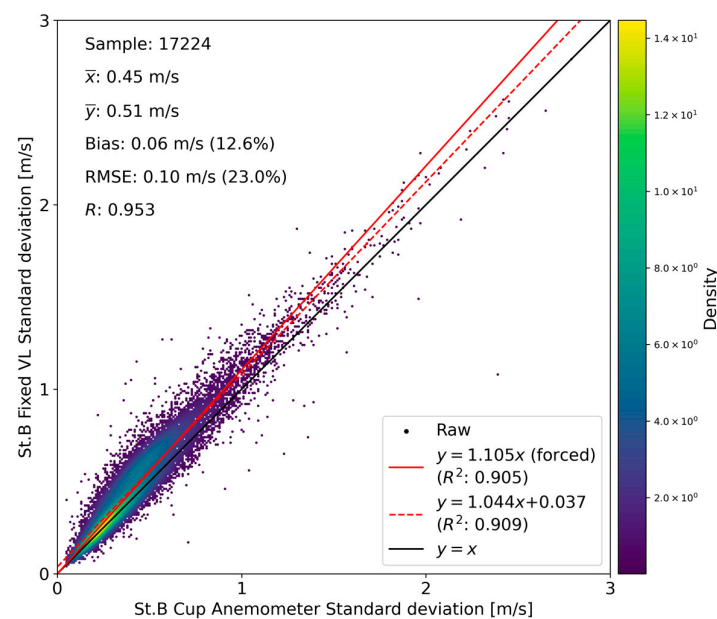


Figure 14. Scatter plot of the SDs from the cup anemometer (x-axis) and VL (y-axis) for the 10 min wind speed range over 2 m/s.

Figure 15 presents the scatter plots of the SDs from the FLSs against the fixed VL or cup anemometer. Only samples of 10 min wind speeds greater than 2 m/s are used. All the units clearly exhibit regression slopes greater than 1, and the large slope is more significant in comparison with the cup anemometer. This result indicates that the FLS significantly overestimates the SD and TI, although the wind speed from the FLS is very similar to that of the cup measurement, as shown earlier. This is consistent with existing studies [12–15]. To exclude a discussion on the systematic error between the cup anemometer and fixed VL, we focus on the bias of the FLS-measured SD against the fixed VL. The bias is found to vary from 7.1% to 97.3%, where the largest bias is observed for FZX, with the smallest for MDB and the median bias for AZX and AWC. This result suggests that the accuracy of the SD depends on the magnitude of the buoy's motion because FZX and MDB are expected to have the largest and smallest buoy motions, respectively.

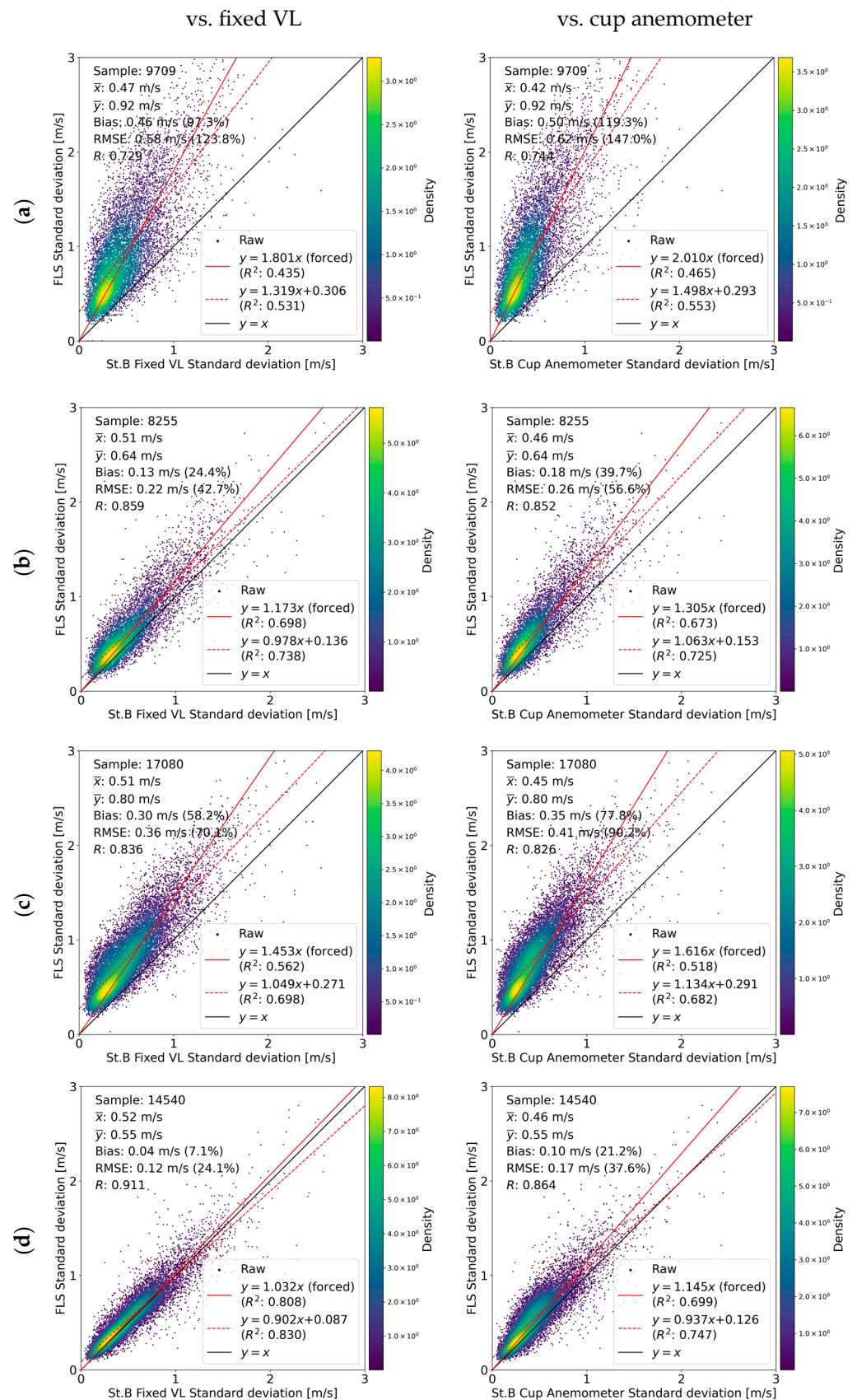


Figure 15. Scatter plots of the SDs for four units for a 10 min wind speed range over 2 m/s (in each plot, the x -axis represents the values obtained for the fixed VL (left) or cup anemometer (right), whereas the y -axis represents those measured using the FLS): (a) FZx, (b) AZx, (c) AWC, and (d) MDB.

Figure 16 presents the TI as a function of the binned wind speed for all four units. The figure only shows the 90-percentile TI values for every 1 m/s bin, as it is commonly used as an input parameter for turbine design. As in Figure 15, the largest SD is observed in the case of FZX, and the smallest for MDB. With respect to the MDB, the FLS-measured TI is almost comparable to the fixed VL-measured TI, although small deviations remain in the low-wind-speed range. In general, the turbine suitability in terms of the ambient TI is considered based on a comparison with the IEC turbulence category. However, as the error in the TI measurement obtained with the FLS exceeds the difference among the IEC categories in some cases, it is difficult to use the FLS-measured TI for turbine conformity studies.

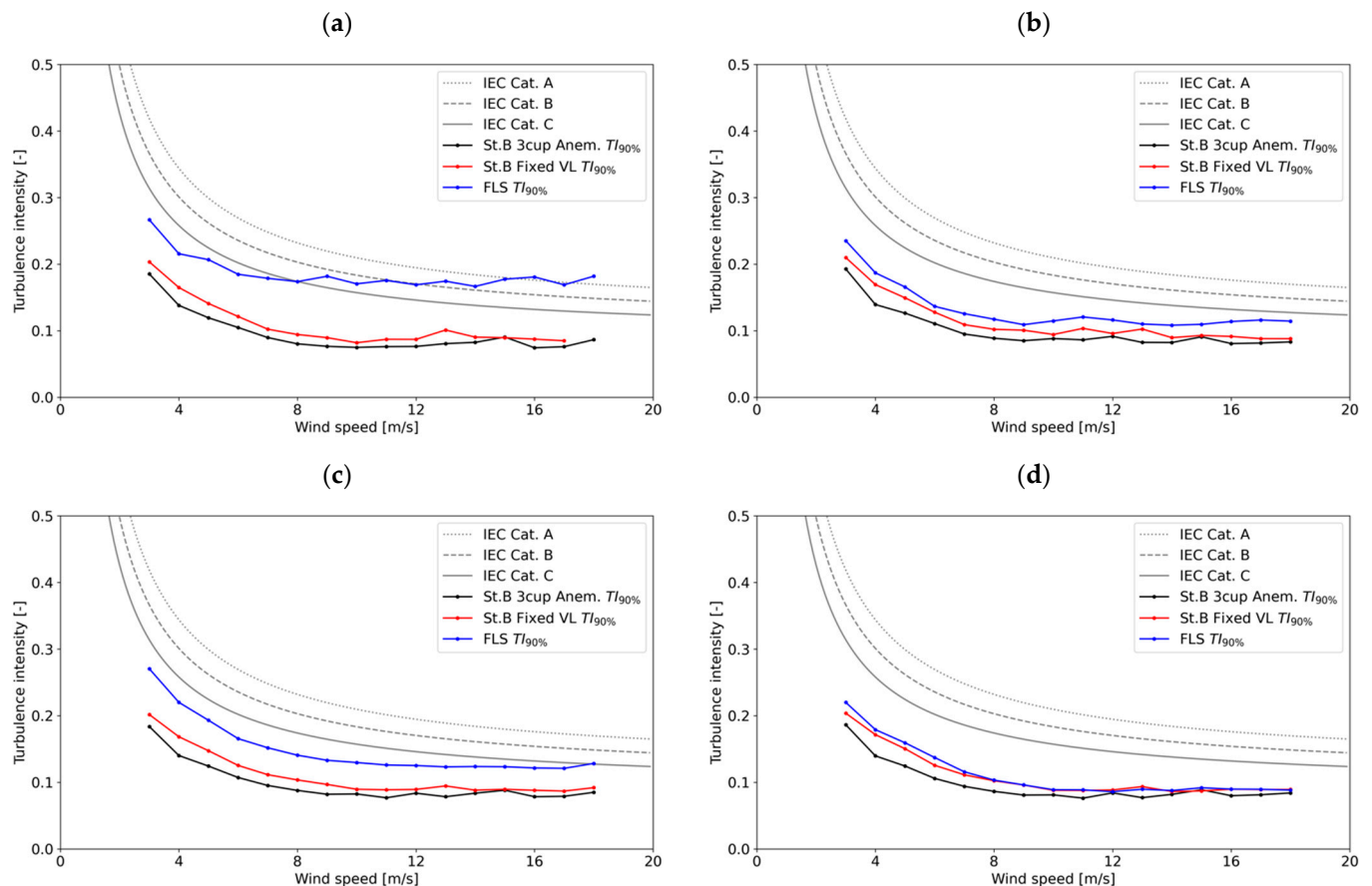


Figure 16. TI as a function of the wind speed at 63 m for four units (the solid black, red, and blue lines indicate the cup-, VL-, and FLS-measured TI, respectively; an IEC normal turbulence model is also presented): (a) FZX, (b) AZX, (c) AWC, and (d) MDB.

Figures 17 and 18 present sensitivity assessments similar to those in Figures 11 and 12 but for the sensitivity of the deviation of the FLS SD from the fixed VL SD to a significant wave period. It should be noted that the reference is a fixed VL instead of a cup anemometer. This direct comparison between “fixed” and “floating” VLs makes more sense as it is unnecessary to take the difference between the VL and cup measurements into consideration, as explained earlier. Figure 17 clearly shows that the sensitivity of the FLS-measured SD to the significant wave height is greater than that of the 10 min wind speed, especially for FZX, AZX, and AWC. This tendency indicates that the greater the wave height that the buoy encounters, the larger the positive bias of the SD. The steepest slope, which indicates the highest sensitivity to the wave height, is confirmed in the case of FZX, which struggles with large motions owing to its smaller buoy shape. In contrast, the MDA-measured SD does not appear to be sensitive to the wave height. In general, the greater the wave height encountered by the buoy, the more significant the buoy’s motion.

Thus, the spatial measurement volume of the LiDAR is significantly changed, resulting in an overestimated SD. This phenomenon is illustrated in Figure 17. As shown in the FZX plot in Figure 18, a smaller wave period also contributes to the overestimated SD, but this may be related to the Fugro buoy being more easily affected by the water level change and wave steepness than the others. For the other FLSs, the wave period affects the SD accuracy less significantly than the wave height. Therefore, the main cause of the overestimated SD and TI values is the wave height. This finding suggests that, when a systematic correction is applied to the FLS for better turbulence measurement, the wave height should be evaluated. In addition, if a low-motion buoy, such as MIA—a spar buoy—is used, the error in the turbulence measurement due to the ocean states may be small or even negligible.

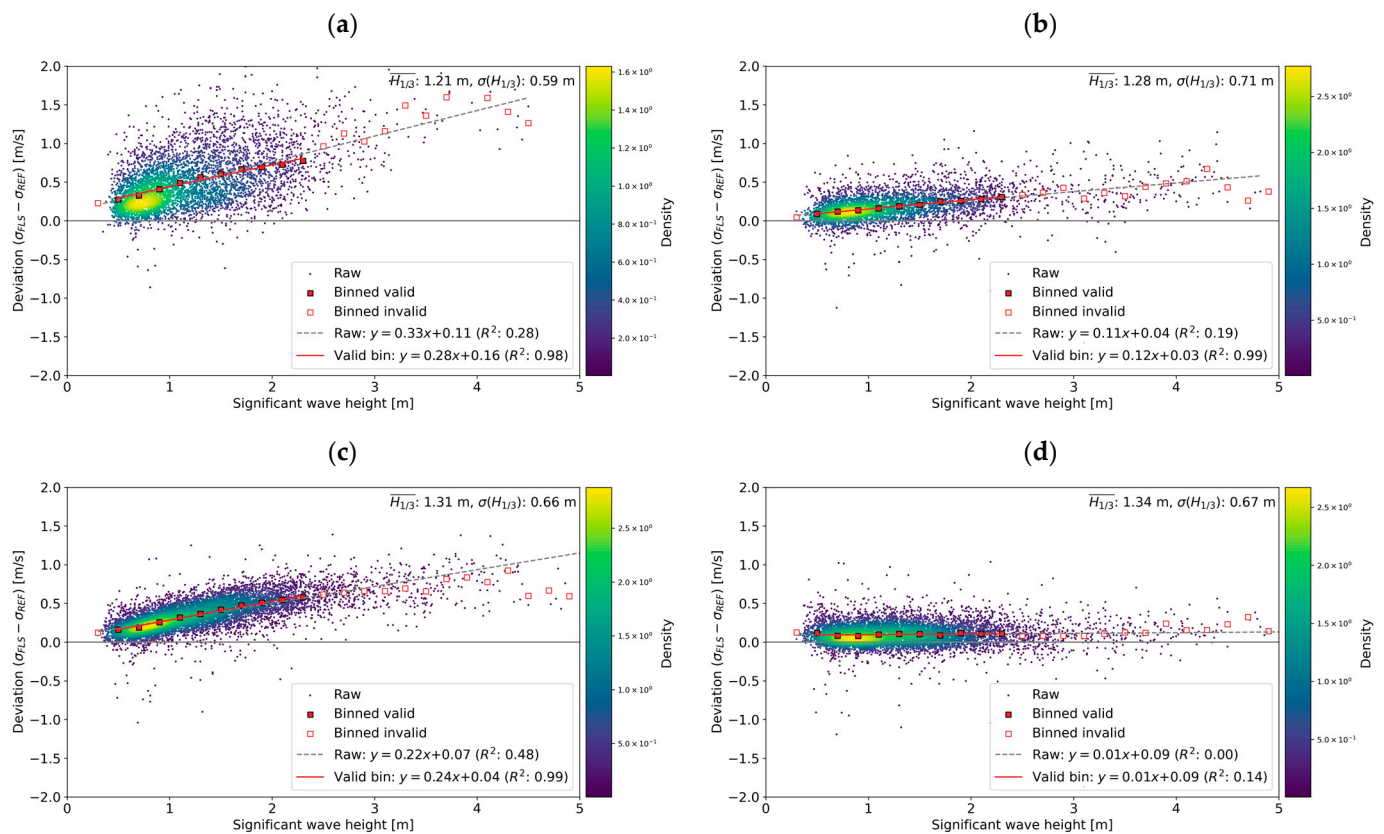


Figure 17. Sensitivity of the deviation of the FLS SD from the fixed VL SD to significant wave height. Only the samples of the 10 min wind speed over 2 m/s are used. The deviation is expressed as an absolute value from the fixed VL SD. The rectangles indicate the averages of the deviation for wind speed bins of a 0.2 m width, and valid values are indicated in red. The gray and red lines indicate regression lines for the raw samples and valid bin averages, respectively. The average and standard deviation of significant wave height are also presented in the figures. (a) FZX, (b) AZX, (c) AWC, and (d) MDB.

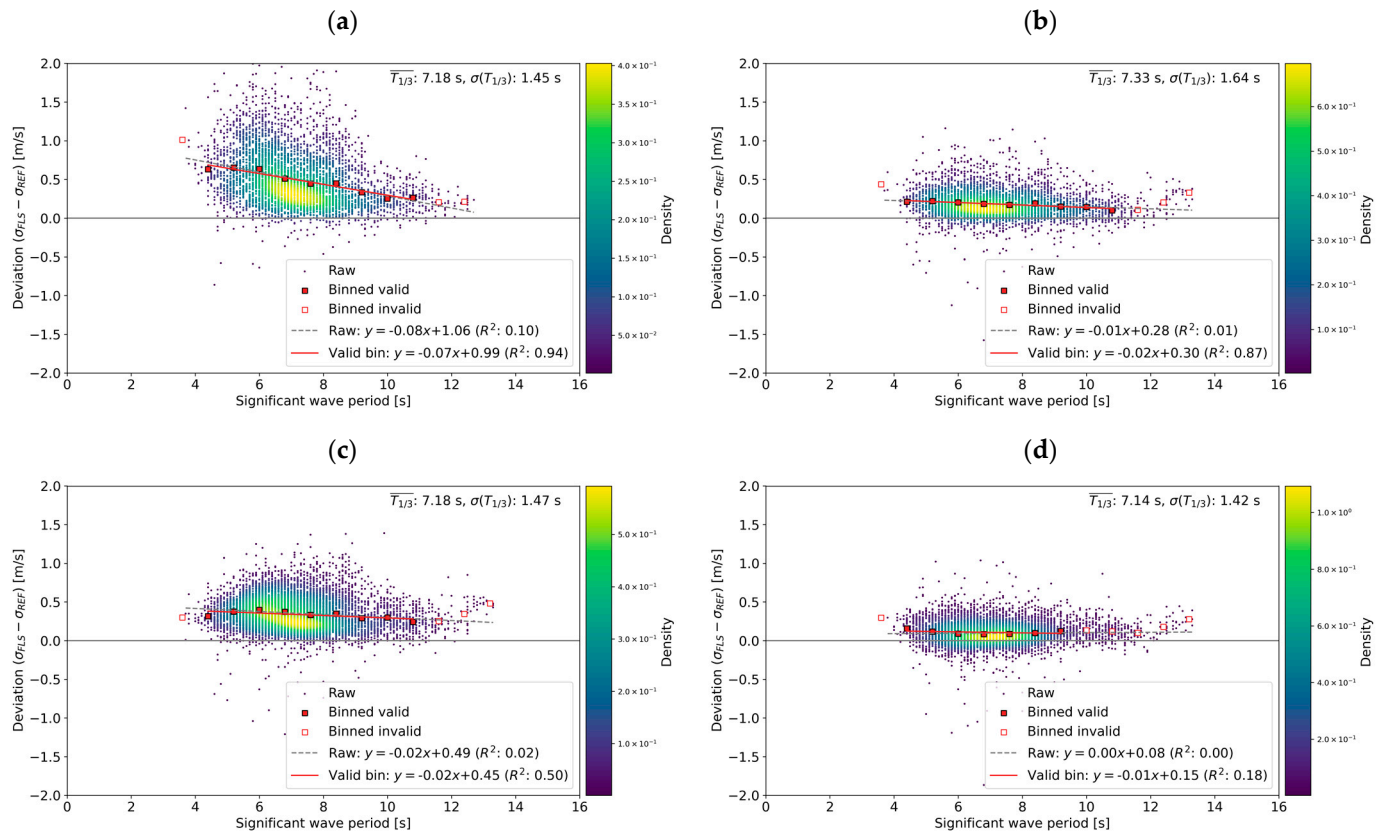


Figure 18. Same as Figure 17, but for the sensitivity to the peak period (bin width is set as 0.8 s): (a) FZX, (b) AZX, (c) AWC, and (d) MDB.

4. Discussion

This study was conducted using four FLS datasets on three different buoys at the Mutsu-Ogawara site in Japan to investigate the performance of FLSs over a region in which little research has been conducted but which has different metocean conditions to Europe, i.e., the main research field.

The performance of the FLS was first investigated in the context of the OWA KPIs in terms of the operational stability/robustness and accuracy of the measured 10 min wind speed and direction. The system and data availabilities were found to not always be satisfactory for meeting the KPIs. Poor system availability was the main cause of the poor data availability, suggesting that there is a need for further improvement in the buoy and robustness of the LiDAR system. In addition, for a successful measurement campaign, it is essential to ensure that an appropriate operation and maintenance plan is in place, in addition to measurement accuracy. The accuracy of the 10 min wind speed and direction was confirmed to be mostly comparable to the best practice defined in the OWA document. This positive result will encourage the use of the FLS for wind resource assessment in Japan and potentially all over the Asia-Pacific region. A detailed sensitivity study focusing on the ocean states revealed that the accuracy of the FLS-measured wind speed is occasionally affected by the wave height but not by the wave period, thus suggesting two possible solutions for further accuracy improvement. One solution is the use of a low-motion buoy, such as a spar-type buoy, to minimize the impact of waves. The second is the development and application of a motion compensation algorithm to eliminate the effects of the motion from the measurement. It is worth mentioning that the former conclusion can only be arrived at using multiple FLSs at the same location, as in this study.

The accuracy of the FLS-measured turbulence component was then verified by considering the difference in the measurement algorithms of the LiDAR and cup anemometer. As expected, the SD and TI with the FLS are largely overestimated compared with the

reference fixed LiDAR and cup anemometer, although the fixed LiDAR also exhibited a slight overestimation derived from the measurement algorithm. In this case, the required specification of wind turbine and its foundation may be overestimated. Also, the wind farm wake loss may be underestimated. The extent of the overestimation strongly depends on the buoy motion, given that the largest and smallest errors are observed in the cases of FZX and MDB, respectively. In addition, harsh wave conditions can worsen the accuracy, particularly for smaller buoys that are sensitive to the wave height. This is because every line-of-sight raw measurement is contaminated with the pointing error and the Doppler effect owing to the rotational and translational motions, respectively. Furthermore, the impact is considerably larger than that in the case of a 10 min averaged wind speed and direction, as only the averaging process can offset the overestimation and underestimation occurring in every raw line-of-sight measurement. This encourages motion compensation development for a better understanding of the turbulent component and 10 min averaged wind speed and the development of a low-motion buoy. For actual use in the design of an offshore wind turbine, it is important to investigate the systematic error of the turbulence measurement that appears in a fixed VL against a cup anemometer owing to the nature of the measurement.

5. Conclusions

In this study, we investigated the performance of four independent wind measurements from three FLSs with different shapes, motions, and measurement systems at the Mutsu-Ogawara port observatory site in Japan. The results obtained are summarized as follows.

The verification of the system and data availability of the FLSs confirmed that the system and data availabilities at 63 m vary from 64.5% to 98.0% and 62.7% to 98.0%, respectively, suggesting that the main factor influencing poor availability is the lack of robustness of the buoy and LiDAR systems rather than environmental reasons.

The 10 min averaged wind speed and direction from the FLSs exhibited sufficient agreement with the reference measurement to achieve the OWA KPIs for the majority of cases, suggesting that the FLS is a reliable measurement tool for resource assessment purposes.

The capability of the FLS for measuring the turbulence components, such as the SD and TI, must be further improved because the FLS measurements still have a large gap from the reference cup anemometer, particularly in the case of a small buoy that is easily affected by the wave conditions.

Having said that, this paper offers users of the FLS technology an overview of how it can be a main source of wind data for an offshore wind resource assessment in Japan. However, the users may need to understand the difficulties in maintaining the higher system and data availability, and the limitation of the turbulence measurement.

This study, with multiple concurrent FLS measurements, revealed differences in the performance of FLS units and deepened our understanding of the measurement characteristics of the FLS in the case of turbulence. These results will aid in the investigation of methods for improving the accuracy of not only the FLS-measured wind speed and direction but also the turbulence components. At the same time, it should be noted that the findings discussed here may not be applicable to other sites in Japan since the campaign has only been conducted at the Mutsu-Ogawara site. Further assessments in a broader region of Japan are needed to have more confidence in understanding the FLS capabilities.

Author Contributions: Conceptualization, S.U. and T.O.; methodology, S.U.; validation, T.O.; formal analysis, S.U.; data curation, H.A., M.K., T.M., R.A. and K.H.; investigation, H.A., M.K., T.M., R.A. and K.H.; writing—original draft preparation, S.U.; writing—review and editing, T.O., H.A., M.K., T.M., R.A. and K.H.; visualization, S.U.; supervision, T.O.; project administration, T.O.; funding acquisition, T.O. and M.K. All authors have read and agreed to the published version of the manuscript.

Funding: This research was funded by the New Energy and Industrial Technology Development Organization (NEDO), Japan (grant number JPNP07015).

Data Availability Statement: Data from the Mutsu-Ogawara Port observatory site (St. B and all FLSs) were collected as part of the NEDO project. The wave data were obtained from the NOWPHAS website (https://www.mlit.go.jp/kowan/nowphas/index_eng.html, accessed on 12 June 2024).

Acknowledgments: This research was the result of the New Energy and Industrial Technology Development Organization (NEDO) project (JPNP07015) and was supported by project members, including the National Institute of Advanced Industrial Science and Technology (AIST), Kobe University, E&E Solutions Inc., Japan Meteorological Corporation, Nippon Kaiji Kyokai (Class NK), and Wind Energy Consulting Inc. In addition, technical support was provided by FLS suppliers (Fugro Group, AXYS Technologies Inc., Japan Meteorological Corporation, and Nagasaki 5 companies). The authors are grateful to the above parties for their support in the research and the writing of this paper.

Conflicts of Interest: Author Shogo Uchiyama was employed by RWE Renewables Japan G.K. Author Hiroshi Asou was employed by International Meteorological & Oceanographic Consultants Co., Ltd. Authors Mizuki Konagaya and Takeshi Misaki were employed by Rera Tech Inc. Author Ryuzo Araki was employed by Japan Meteorological Corporation. Author Kohei Hamada was employed by E&E Solutions Inc. The remaining author declares that the research was conducted in the absence of any commercial or financial relationships that could be construed as a potential conflict of interest. In addition, the authors have no intention of influencing the readers' choice or promoting any specific FLS model, including but not limited to those discussed in this study.

References

1. Gottschall, J.; Wolken-Möhlmann, G.; Viergutz, T.; Lange, B. Results and conclusions of a floating-lidar offshore test. *Energy Procedia* **2014**, *53*, 156–161. [CrossRef]
2. Gottschall, J.; Gribben, B.; Stein, D.; Würth, I. Floating lidar as an advanced offshore wind speed measurement technique: Current technology status and gap analysis in regard to full maturity. *Wiley Interdiscip. Rev. Energy Environ.* **2017**, *6*, e250. [CrossRef]
3. Vepa, K.S.; Duffey, T.; Paeppegem, W.V. Gyroscope-based floating lidar design proposal for getting stable offshore wind velocity profiles. *Sea Technol.* **2016**, *57*, 41–43.
4. Bischoff, O.; Würth, I.; Gottschall, J.; Gribben, B.; Hughes, J.; Stein, D.; Verhoef, H. *IEA Wind, Expert Group Report on Recommended Practices, 18. Floating LiDAR Systems*, 1st ed.; IEA Wind: Paris, France, 2017.
5. Mathisen, J.-P. Measurement of Wind Profile with a Buoy Mounted Lidar. 2013; p. 19. Available online: https://www.sintef.no/globalassets/project/deepwind-2013/deepwind-presentations-2013/c2/mathisen-j.p_fugro-oceanor.pdf (accessed on 12 June 2024).
6. Bischoff, O.; Würth, I.; Cheng, P.; Tiana-Alsina, J.; Gutiérrez, M. Motion effects on lidar wind measurement data of the EOLOS buoy. In Proceedings of the First International Conference on Renewable Energies Offshore, Lisbon, Portugal, 24–26 November 2014.
7. Bischoff, O.; Yu, W.; Gottschall, J.; Cheng, P.W. Validating a simulation environment for floating lidar systems. *J. Phys. Conf. Ser.* **2018**, *1037*, 052036. [CrossRef]
8. Bastigkeit, I.; Leimeister, M.; Watson, W.; Wolken-Möhlmann, G.; Gottschall, J. Enhanced design basis for offshore wind farm load calculations based on met-ocean data from a floating lidar system. *J. Phys. Conf. Ser.* **2021**, *2018*, 012008. [CrossRef]
9. Carbon Trust Offshore Wind Accelerator (OWA). Roadmap for the Commercial Acceptance of Floating Lidar Technology. 2018. Available online: <https://ctprodstorageaccountp.blob.core.windows.net/prod-drupal-files/documents/resource/public/Roadmap%20for%20Commercial%20Acceptance%20of%20Floating%20LiDAR%20REPORT.pdf> (accessed on 12 June 2024).
10. Viselli, A.; Filippelli, M.; Pettigrew, N.; Dagher, H.; Faessler, N. Validation of the first LiDAR wind resource assessment buoy system offshore the Northeast United States. *Wind Energy* **2019**, *22*, 1548–1562. [CrossRef]
11. Gutiérrez-Antuñano, M.A.; Tiana-Alsina, J.; Rocadenbosch, F. Performance evaluation of a floating lidar buoy in nearshore conditions. *Wind Energy* **2017**, *20*, 1711–1726. [CrossRef]
12. Gottschall, J.; Wolken-Möhlmann, G.; Lange, B. About offshore resource assessment with floating lidars with special respect to turbulence and extreme events. *J. Phys. Conf. Ser.* **2014**, *555*, 012043. [CrossRef]
13. Gutiérrez-Antuñano, M.A.; Tiana-Alsina, J.; Salcedo, A.; Rocadenbosch, F. Estimation of the motion-induced-horizontal-wind-speed standard deviation in an offshore Doppler lidar. *Remote Sens.* **2018**, *10*, 2037. [CrossRef]
14. Kelberlau, F.; Neshaug, V.; Lonseth, L.; Bracchi, T.; Mann, J. Taking the motion out of floating lidar: Turbulence intensity estimates with a continuous-wave wind lidar. *Remote Sens.* **2020**, *12*, 898. [CrossRef]
15. Yamaguchi, A.; Ishihara, T. A new motion compensation algorithm of floating lidar system for the assessment of turbulence intensity. *J. Phys. Conf. Ser.* **2016**, *753*, 072034. [CrossRef]
16. Ohsawa, T.; Shimada, S.; Kogaki, T.; Iwashita, T.; Konagaya, M.; Araki, R.; Imamura, H. Progress of NEDO project “Bottom fixed offshore wind farm development support project (Establishment of offshore wind resource assessment method)”. *Proc. Jpn. Wind. Energy Symp.* **2020**, *42*, 136–139. (In Japanese)
17. The Nationwide Ocean Wave Information Network for Ports and HarbourS (NOWPHAS). Available online: https://www.mlit.go.jp/kowan/nowphas/index_eng.html (accessed on 29 March 2024).

18. Konagaya, M.; Ohsawa, T.; Inoue, T.; Mito, T.; Kato, H.; Kawamoto, K. Land–Sea Contrast of Nearshore Wind Conditions: Case Study in Mutsu-Ogawara. *SOLA* **2021**, *17*, 234–238. [[CrossRef](#)]
19. Türk, M.; Emeis, S. The dependence of offshore turbulence intensity on wind speed. *J. Wind Eng. Ind. Aerodyn.* **2010**, *98*, 466–471. [[CrossRef](#)]
20. IEC 61400-12-1; Ed. 2.0 Wind Energy Generation Systems—Part 12-1: Power Performance Measurements of Electricity Producing Wind Turbines. International Electrotechnical Commission: Geneva, Switzerland, 2017.
21. Wagner, R.; Mikkelsen, T.; Courtney, M. *Investigation of Turbulence Measurements with a Continuous Wave, Conically Scanning LiDAR*; Technical University of Denmark: Kongens Lyngby, Denmark, 2009; Technical Report Risø-R-1682(EN), Risø DTU.
22. Sathe, A.; Mann, J. A review of turbulence measurements using ground-based wind lidars. *Atmos. Meas. Tech.* **2013**, *6*, 3147–3167. [[CrossRef](#)]
23. Newman, J.F.; Clifton, A. An error reduction algorithm to improve lidar turbulence estimates for wind energy. *Wind Energy Sci.* **2017**, *2*, 77–95. [[CrossRef](#)]
24. Kelberlau, F.; Mann, J. Better turbulence spectra from velocity–azimuth display scanning wind lidar. *Atmos. Meas. Tech.* **2019**, *12*, 1871–1888. [[CrossRef](#)]

Disclaimer/Publisher’s Note: The statements, opinions and data contained in all publications are solely those of the individual author(s) and contributor(s) and not of MDPI and/or the editor(s). MDPI and/or the editor(s) disclaim responsibility for any injury to people or property resulting from any ideas, methods, instructions or products referred to in the content.